1996ApJ...470..364E

THE ASTROPHYSICAL JOURNAL, 470:364–377, 1996 October 10
© 1996. The American Astronomical Society. All rights reserved. Printed in U.S.A.

MULTIWAVELENGTH OBSERVATIONS OF SHORT-TIMESCALE VARIABILITY IN NGC 4151. IV. ANALYSIS OF MULTIWAVELENGTH CONTINUUM VARIABILITY

R. A. EDELSON,[1] T. ALEXANDER,[2] D. M. CRENSHAW,[3] S. KASPI,[2] M. A. MALKAN,[4] B. M. PETERSON,[5] R. S. WARWICK,[6] J. CLAVEL,[7] A. V. FILIPPENKO,[8] K. HORNE,[9] K. T. KORISTA,[10] G. A. KRISS,[11] J. H. KROLIK,[11] D. MAOZ,[2] K. NANDRA,[12] P. T. O'BRIEN,[6] S. V. PENTON,[13] T. YAQOOB,[12] P. ALBRECHT,[14] D. ALLOIN,[15] T. R. AYRES,[13] T. J. BALONEK,[16] P. BARR,[7] A. J. BARTH,[8] R. BERTRAM,[5,17] G. E. BROMAGE,[6] M. CARINI,[18] T. E. CARONE,[19,20] F.-Z. CHENG,[21] K. K. CHUVAEV,[22,23] M. DIETRICH,[24] D. DULTZIN-HACYAN,[25] C. M. GASKELL,[26] I. S. GLASS,[27] M. R. GOAD,[28] S. HEMAR,[2] L. C. HO,[29] J. P. HUCHRA,[29] J. HUTCHINGS,[30] W. N. JOHNSON,[31] D. KAZANAS,[12] W. KOLLATSCHNY,[14] A. P. KORATKAR,[28] O. KOVO,[2] A. LAOR,[32] G. M. MACALPINE,[33] P. MAGDZIARZ,[34] P. G. MARTIN,[35] T. MATHESON,[8] B. MCCOLLUM,[18] H. R. MILLER,[36] S. L. MORRIS,[30] V. L. OKNYANSKIJ,[37] J. PENFOLD,[38] E. PÉREZ,[28] G. C. PEROLA,[39] G. PIKE,[12,40] R. W. POGGE,[5] R. L. PTAK,[41] B.-C. QIAN,[42] M. C. RECONDO-GONZÁLEZ,[43] G. A. REICHERT,[44] J. M. RODRÍGUEZ-ESPINOZA,[45] P. M. RODRÍGUEZ-PASCUAL,[46] E. L. ROKAKI,[47] J. ROLAND,[48] A. C. SADUN,[49] I. SALAMANCA,[50] M. SANTOS-LLEÓ,[51] J. C. SHIELDS,[52,53] J. M. SHULL,[13,54] D. A. SMITH,[6] S. M. SMITH,[5] M. A. J. SNIJDERS,[55,56] G. M. STIRPE,[57] R. E. STONER,[41] W.-H. SUN,[58] M.-H. ULRICH,[59] E. VAN GRONINGEN,[60] R. M. WAGNER,[5,17] S. WAGNER,[24] I. WANDERS,[5] W. F. WELSH,[61] R. J. WEYMANN,[62] B. J. WILKES,[29] H. WU,[63] J. WURSTER,[1] S.-J. XUE,[21] A. A. ZDZIARSKI,[64] W. ZHENG,[11] AND Z.-L. ZOU[63]

Received 1996 March 5; accepted 1996 May 1

ABSTRACT

This paper combines data from the three preceding papers in order to analyze the multi–wave-band variability and spectral energy distribution of the Seyfert 1 galaxy NGC 4151 during the 1993 December monitoring campaign. The source, which was near its peak historical brightness, showed strong, correlated variability at X-ray, ultraviolet, and optical wavelengths. The strongest variations were seen in medium-energy ($\sim$1.5 keV) X-rays, with a normalized variability amplitude (NVA) of 24%. Weaker (NVA = 6%) variations (uncorrelated with those at lower energies) were seen at soft gamma-ray energies of $\sim$100 keV. No significant variability was seen in softer (0.1–1 keV) X-ray bands. In the ultraviolet/optical regime, the NVA decreased from 9% to 1% as the wavelength increased from 1275 to 6900 Å. These data do not probe extreme ultraviolet (1200 Å to 0.1 keV) or hard X-ray (2–50 keV) variability. The phase differences between variations in different bands were consistent with zero lag, with upper limits of $\lesssim$0.15 day between 1275 Å and the other ultraviolet bands, $\lesssim$0.3 day between 1275 Å and 1.5 keV, and $\lesssim$1 day between 1275 and 5125 Å. These tight limits represent more than an order of magnitude improvement over those determined in previous multi–wave-band AGN monitoring campaigns. The ultraviolet fluctuation power spectra showed no evidence for periodicity, but were instead well fitted with a very steep, red power law ($a \leq -2.5$).

If photons emitted at a "primary" wave band are absorbed by nearby material and "reprocessed" to produce emission at a secondary wave band, causality arguments require that variations in the secondary band follow those in the primary band. The tight interband correlation and limits on the ultraviolet and medium-energy X-ray lags indicate that the reprocessing region is smaller than $\sim$0.15 lt-day in size. After correcting for strong (a factor of $\gtrsim$15) line-of-sight absorption, the medium-energy X-ray luminosity variations appear adequate to drive the ultraviolet/optical variations. However, the medium-energy X-ray NVA is 2–4 times that in the ultraviolet, and the single-epoch, absorption-corrected X-ray/gamma-ray luminosity is only about one-third of that of the ultraviolet/optical/infrared, suggesting that at most about a third of the total low-energy flux could be reprocessed high-energy emission.

The strong wavelength dependence of the ultraviolet NVAs is consistent with an origin in an accretion disk, with the variable emission coming from the hotter inner regions and nonvariable emission from the cooler outer regions. These data, when combined with the results of disk fits, indicate a boundary between these regions near a radius of order $R \approx 0.07$ lt-day. No interband lag would be expected, as reprocessing (and thus propagation between regions) need not occur, and the orbital timescale of $\sim$1 day is consistent with the observed variability timescale. However, such a model does not immediately explain the good correlation between ultraviolet and X-ray variations.

Subject headings: galaxies: active — galaxies: individual (NGC 4151) — galaxies: Seyfert — ultraviolet: galaxies — X-rays: galaxies

© American Astronomical Society • Provided by the NASA Astrophysics Data System

1996ApJ...470..364E

1. INTRODUCTION

Two of the most constraining observed properties of active galactic nuclei (AGN) are their large luminosities over a broad range of energies (gamma ray through infrared) and their rapid variability (implying a small source size unless the emission is highly beamed). The inferred large energy densities have led to a standard model of the ultimate energy source being the release of gravitational potential energy of matter from an accretion disk surrounding a supermassive black hole (e.g., Rees 1984). Although this general model has broad support, the specific physical processes that produce the complex, broadband spectral energy distributions (SEDs) observed from AGN have not been clearly identified. It is believed that a mix of processes is important. The ultraviolet and optical emission may be primary radiation from an accretion disk (Shields 1978; Malkan & Sargent 1982; Malkan 1983). In low-luminosity

[1] Department of Physics and Astronomy, 203 Van Allen Hall, University of Iowa, Iowa City, IA 52242; edelson@spacly.physics.uiowa.edu.
[2] School of Physics and Astronomy and Wise Observatory, Raymond and Beverly Sackler Faculty of Exact Sciences, Tel-Aviv University, Tel Aviv 69978, Israel.
[3] Astronomy Program, Computer Sciences Corporation, NASA Goddard Space Flight Center, Code 681, Greenbelt, MD 20771.
[4] Department of Astronomy, University of California, Math-Science Building, Los Angeles, CA 90024.
[5] Department of Astronomy, Ohio State University, 174 West 18th Avenue, Columbus, OH 43210.
[6] Department of Astronomy, University of Leicester, University Road, Leicester LE1 7RH, UK.
[7] ISO Project, European Space Agency, Apartado 50727, 28080 Madrid, Spain.
[8] Department of Astronomy, University of California, Berkeley, CA 94720.
[9] School of Physics and Astronomy, University of St. Andrews, North Haugh, St. Andrews KY169SS, Scotland, UK.
[10] Department of Physics and Astronomy, University of Kentucky, Lexington, KY 40506.
[11] Department of Physics and Astronomy, Johns Hopkins University, Baltimore, MD 21218.
[12] Laboratory for High Energy Astrophysics, NASA Goddard Space Flight Center, Greenbelt, MD 20771.
[13] Center for Astrophysics and Space Astronomy, University of Colorado, Campus Box 389, Boulder CO 80309.
[14] Universitäts-Sternwarte Göttingen, Geismarlandstrasse 11, D-37083 Göttingen, Germany.
[15] Centre d'Etudes de Saclay, Service d'Astrophysique, Orme des Merisiers, 91191 Gif-sur-Yvette Cedex, France.
[16] Department of Physics and Astronomy, Colgate University, Hamilton, NY 13346.
[17] Postal address: Lowell Observatory, 1400 West Mars Hill Road, Flagstaff, AZ 86001.
[18] Computer Sciences Corporation, NASA Goddard Space Flight Center, Code 684.9, Greenbelt, MD 20771.
[19] Space Sciences Laboratory, University of California, Berkeley, CA 94720, and Eureka Scientific, Inc.
[20] Current address: 28740 West Fox River Drive, Cary, IL 60013.
[21] Center for Astrophysics, University of Science and Technology, Hefei, Anhui, People's Republic of China.
[22] Crimean Astrophysical Observatory, P/O Nauchny, 334413, Crimea, Ukraine.
[23] Deceased 1994 November 15.
[24] Landessternwarte, Königstuhl, D-69117 Heidelberg, Germany.
[25] Universidad Nacional Autónoma de Mexico, Instituto de Astronomía, Apartado Postal 70-264, 04510 México D. F., Mexico.
[26] Department of Physics and Astronomy, University of Nebraska, Lincoln, NE 68588.
[27] South African Astronomical Observatory, P.O. Box 9, Observatory 7935, South Africa.
[28] Space Telescope Science Institute, 3700 San Martin Drive, Baltimore, MD 21218.
[29] Harvard-Smithsonian Center for Astrophysics, 60 Garden Street, Cambridge, MA 02138.
[30] Dominion Astrophysical Observatory, 5071 West Saanich Road, Victoria, BC V8X 4M6, Canada.
[31] Naval Research Laboratory, Code 4151, 4555 Overlook Avenue, SW, Washington, DC 20375-5320.
[32] Physics Department, Technion–Israel Institute of Technology, Haifa 32000, Israel.
[33] Department of Astronomy, University of Michigan, Dennison Building, Ann Arbor, M1 48109.
[34] Astronomical Observatory, Jagiellonian University, Orla 171, 30-244 Cracow, Poland.
[35] Canadian Institute for Theoretical Astrophysics, University of Toronto, Toronto, ON M5S 1A1, Canada.
[36] Department of Physics and Astronomy, Georgia State University, Atlanta, GA 30303.
[37] Sternberg Astronomical Institute, University of Moscow, Universitetskij Prosp. 13, Moscow 119899, Russia.
[38] Department of Physics and Astronomy, University of Calgary, 2500 University Drive NW, Calgary, AB T2N 1N4, Canada; and Department of Mathematics, Physics, and Engineering, Mount Royal College, Calgary T3E 6K6, Canada.
[39] Istituto Astronomico dell'Università, via Lancisi 29, I-00161 Rome, Italy.
[40] Postal address: 816 S. La Grange Road, La Grange, IL 60525.
[41] Department of Physics and Astronomy, Bowling Green State University, Bowling Green, OH 43403.
[42] Shanghai Observatory, Chinese Academy of Sciences, People's Republic of China.
[43] Facultad de Ciencias, Departimento Físicas, Universidad de Oviedo, C/Calvo Sotelo, s/n Oviedo, Asturias, Spain.
[44] NASA Goddard Space Flight Center, Code 631, Greenbelt, MD 20771.
[45] Instituto de Astrofísica de Canarias, E-38200 La Laguna, Tenerife, Spain.
[46] ESA *IUE* Observatory, P.O. Box 50727, 28080 Madrid, Spain.
[47] Royal Observatory Edinburgh, University of Edinburgh, Blackford Hill, Edinburgh EH9 3HJ, UK.
[48] Institut d'Astrophysique, 98 bis boulevard Arago, F-75014 Paris, France.
[49] Department of Physics and Astronomy and Bradley Observatory, Agnes Scott College, Decatur, GA 30030.
[50] Royal Greenwich Observatory, Madingley Road, Cambridge, CB3 0EZ, UK.
[51] LAEFF, Apartado 50727, E-28080 Madrid, Spain.
[52] Steward Observatory, University of Arizona, Tucson, AZ 85726.
[53] Hubble Fellow.
[54] JILA; University of Colorado and National Institute of Standards and Technology, Campus Box 440, Boulder, CO 80309.
[55] IRAM, 300 rue de la Piscine, 38046 St. Martin d'Hères, France.
[56] Postal address: rue Elysée Reclubus 1 bis, 38100 Grenoble, France.
[57] Osservatorio Astronomico di Bologna, via Zamboni 33, I-40126, Bologna, Italy.
[58] Institute of Astronomy, National Central University, Chung-Li, Taiwan 32054, Republic of China.
[59] European Southern Observatory, Karl-Schwarzschild-Strasse 2, 85748 Garching, Germany.
[60] Astronomiska Observatoriet, Box 515, S-751 20 Uppsala, Sweden.
[61] Department of Physics, Keele University, Keele ST5 5BG, Staffordshire, UK.
[62] Observatories of the Carnegie Institution of Washington, 813 Santa Barbara Street, Pasadena, CA 91101.
[63] Beijing Astronomical Observatory, Chinese Academy of Sciences, Beijing 100080, People's Republic of China.
[64] N. Copernicus Astronomical Center, Bartycka 18, 00-716 Warsaw, Poland.

© American Astronomical Society • Provided by the NASA Astrophysics Data System

1996ApJ...470..364E

objects starlight will contribute as well. Thermal dust emission is an important ingredient of the infrared band (Barvainis 1987; Sanders et al. 1989). The high-energy (X-ray and gamma ray) emission is not well understood. There are a variety of models for their origin, ranging from electromagnetic cascades in an e^+e^- pair plasma (Zdziarski et al 1990) to thermal Comptonization models (Haardt & Maraschi 1993; Haardt, Maraschi, & Ghisellini 1994). Furthermore, gas near the central source may reprocess at least some of the primary radiation via Compton scattering, absorption, and fluorescent processes (Guilbert & Rees 1988; Lightman & White 1988; George & Fabian 1991; Matt, Fabian, & Ross 1993).

Determination of the mix of physical processes that produce these large, broadband luminosities is a major unresolved issue in AGN research, and multi–wave-band variability studies are potentially highly constraining. Causality arguments imply that if emission in a "secondary" band is produced when photons from a "primary" band are reprocessed in material near the central engine, then variations in the secondary band could not be seen to lead those in the primary band. Furthermore, if the emission in any given wave band is a combination of two independent components (with presumably independent variability behavior), then measurement of broadband spectral variability might allow them to be separated. Finally, if a characteristic variability timescale could be measured, it could be compared with those indicative of different physical processes (e.g., with the expected viscous, orbital, and light-travel timescales).

In spite of the potential power of this approach, it has not until recently been exploited because of the very large amount of telescope time required. In several experiments designed to measure the size of the broad-line region in the Seyfert 1 galaxy NGC 5548, variations at $\sim$1400 Å were seen to track those at $\sim$2800 and $\sim$5000 Å to within $\lesssim$1–2 days (Clavel et al. 1991; Peterson et al. 1991; Korista et al. 1995). This was taken to imply an ultraviolet-optical propagation time that is too short to be associated with any dynamics mediated by viscosity, such as variations in the mass inflow rate, in a standard α-disk (Krolik et al. 1991; but see § 4.2 below). Similar problems were noted in ultraviolet and optical monitoring of NGC 4151 by Ulrich et al. (1991). Krolik et al. (1991) suggested that variation in the different wave bands in NGC 5548 were coordinated by a photon signal. Nandra et al. (1991) suggested that this signal might be X-ray heating (reprocessing). Several authors constructed specific models of X-ray–illuminated accretion disks to acount for the NGC 5548 data (Collin-Souffrin 1991; Rokaki & Magnan 1992; Molendi, Maraschi, & Stella 1992; Rokaki, Collin-Souffrin, & Magnan 1993) as well as for NGC 4151 (Perola & Piro 1994). A strong test of the idea that the ultraviolet is produced by reprocessing X-ray photons could be made by measuring the time relationship between fluctuations in the ultraviolet and the X-rays, but previous attempts (e.g., Clavel et al. 1992) lacked adequate temporal resolution.

In order to attempt this test, an international consortium of AGN observers undertook a campaign to intensively monitor a single Seyfert 1 galaxy, NGC 4151, at ultraviolet, X-ray, gamma-ray and optical wavelengths for $\sim$10 days in 1993 December. These data are described in detail in the three preceding papers (Paper I, Crenshaw et al. 1996; Paper II, Kaspi et al. 1996; and Paper III, Warwick et al. 1996); they are summarized in the following section. In this paper, the multiwavelength data are analyzed in combination. The measurement of the multi–wave-band variability, temporal correlations, phase lags, and the broadband optical–through–gamma-ray SED are analyzed in § 3, and the scientific implications are briefly discussed in § 4.

2. DATA

The aim of these observations was to monitor NGC 4151 intensively across the accessible optical–through–gamma-ray region during the period from MJD 22.5 to MJD 32.2. (The modified Julian Date, MJD, is defined as MJD = JD − 2,449,300. All dates refer to the center points of observations unless otherwise noted.) While scheduling difficulties, satellite malfunctions, and other minor problems did cause some gaps and perturbations in this plan, this campaign still produced the most intensive coordinated observations to date of an AGN across these high-energy wave bands. Along with daily observations before and after this period (not analyzed in this paper), the *International Ultraviolet Explorer* (*IUE*) observed NGC 4151 nearly continuously from MJD 22.6 to MJD 31.9. A pair of SWP and LWP spectra, spanning the range 1200–2000 Å and 2000–3000 Å, respectively, was obtained every $\sim$70 minutes, excluding a daily $\sim$2 hr gap at about modulo MJD 0.4–0.5. *ROSAT* observed the source twice per day, with nearly even sampling from MJD 22.5 to MJD 28.0. A satellite malfunction caused *ROSAT* to go into safe mode for most of the second half of the campaign, although it did make one final observation at MJD 32.2. *ASCA* was also plagued by satellite problems (this time in the first half of the campaign) but four 10 ks observations were successfully obtained at MJD 26.0, 27.5, 29.1, and 31.6. *Compton Gamma Ray Observatory* (*CGRO*) observations were made with the OSSE instrument during the period MJD 22.7–34.6. Ground-based optical spectra were obtained for a 2 month period that included these dates. Figure 1 gives the light curves in nominal 100 keV, 1.5 keV, 1275 Å, 1820 Å, 2688 Å, and 5125 Å wave bands. These bands are explicitly defined below, and further details of the sampling characteristics are given in Table 1.

A total of 18 optical spectra were obtained during the intensive monitoring period; 10 at Perkins Observatory (Ohio State University) and eight at Wise Observatory. The Wise data covered 4210–6990 Å with $\sim$5 Å resolution through a 10″ slit, while the OSU data covered 4480–5660 Å at $\sim$9 Å resolution through a 5″ slit. These data were intercalibrated to remove the effects of (presumably nonvariable) extended emission and instrumental offsets from the light curves. Continuum fluxes in the 4600 ± 40 and 5125 ± 25 Å bands and Hβ line fluxes were measured from both sets of spectra, while 6200 ± 30 and 6925 ± 25 Å continuum fluxes and Hα line fluxes were measured only from the Wise data. The Wise spectrograph projects to 10″ × 13″ on the sky, and approximately 25% of the light at

TABLE 1

SAMPLING CHARACTERISTICS

Light Curve	Number of Epochs	Δt_{ave} (days)	Δt_{median} (days)
1275 Å, 1820 Å.....	176	0.053 ± 0.022	0.046
2688 Å	168	0.055 ± 0.025	0.046
Soft X-ray	17	0.607 ± 0.540	0.500
5125 Å	18	0.549 ± 0.250	0.585

© American Astronomical Society • Provided by the NASA Astrophysics Data System

1996ApJ...470..364E

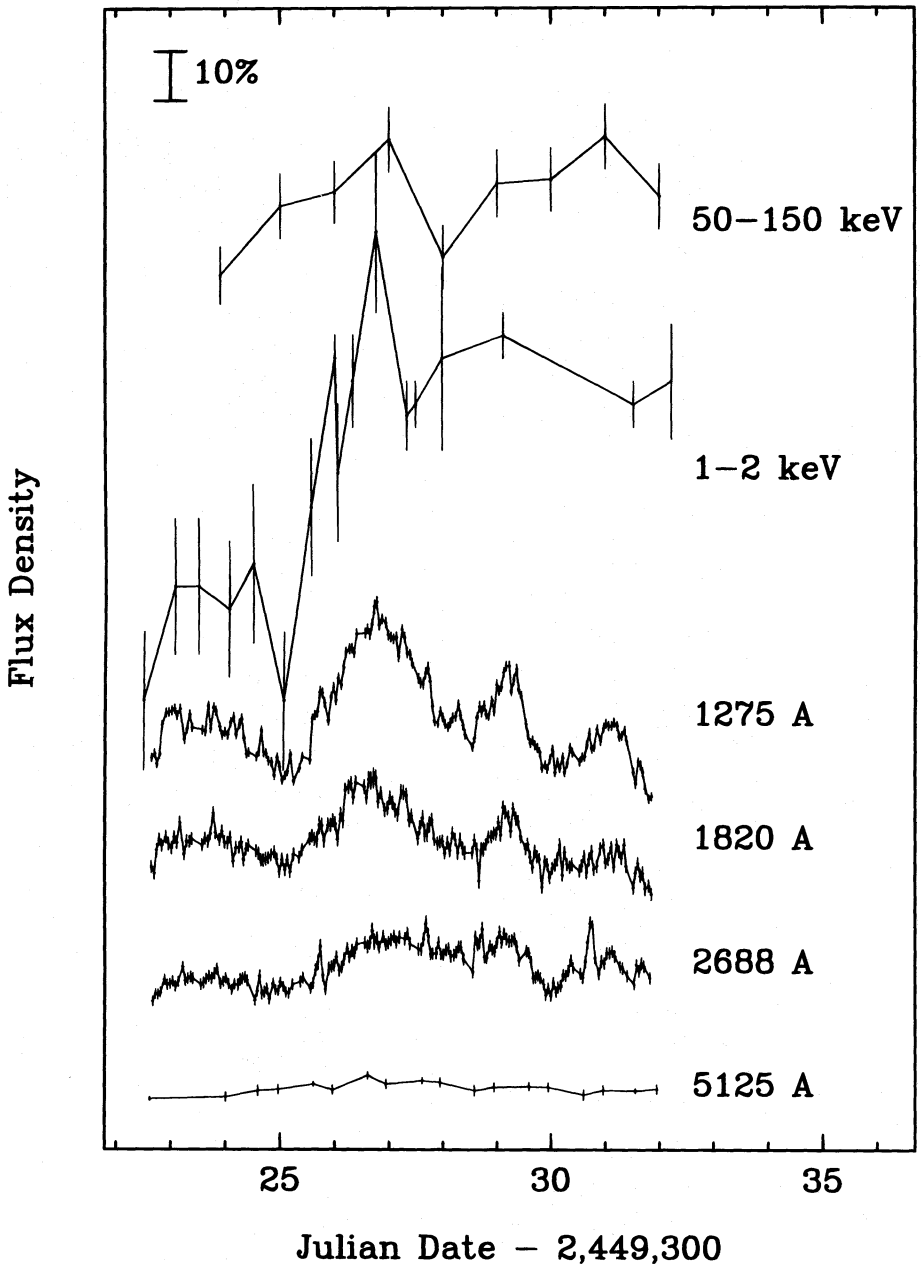

FIG. 1.—Continuum light curves during the 10 day intensive monitoring period, for wave bands centered on 100 keV, 1.5 keV, 1275 Å, 1820 Å, 2688 Å, and 5125 Å. The light curves are on a common scale, but shifted in flux to present them in one figure, so a 10% flux change is shown. The X-ray data showed the strongest variability but the poorest sampling; the interruption in the second half of the campaign was due to a spacecraft malfunction. The apparent short flares in the 2688 Å light curve are probably due to instrumental effects and not intrinsic variability.

a wavelength of 5125 Å is due to starlight from the host galaxy (see § 3.5). The uncertainties in measurements of the optical fluxes are at about the 1% level (see Paper II for details). The 5125 Å data from both telescopes were combined in the correlation analyses and light curves.

During the intensive monitoring period, *IUE* obtained a total of 176 spectra with the SWP camera and 168 with the LWP camera. Observations were spaced as closely as possible, leading to fairly even sampling of ~18 spectra per day in each camera, with a ~2 hr period each day, during which no data were obtained because of Earth occultation and high particle background. One-dimensional spectra were extracted using the TOMSIPS package (Ayres 1993). Continuum fluxes were measured by summing over relatively line-free, ~30 Å wide bands centered at 1275, 1330, 1440, 1820, 1950, 2300, and 2688 Å. Uncertainties, taken to be the standard error in the band, were typically 1%–2%, consistent with the observed epoch-to-epoch dispersion in the measured fluxes. Line fluxes (C IV, He II, and C III]) were measured by fitting multiple Gaussians. (See Paper I and Penton et al. 1996 for details of the *IUE* data reduction.) The continuum light curves measured at 1275, 1820, 2688, and 5125 Å were used in the light curves and time-series analyses, all of the ultraviolet/optical continuum data were used only in the variability amplitude and zero-lag correlation analyses, and the emission-line data were not used in this paper.

The *ROSAT* PSPC made a total of 13 observations of NGC 4151 between MJD 22.5 and MJD 28.0. Although the center points of the first 12 observations were almost evenly

© American Astronomical Society • Provided by the NASA Astrophysics Data System

1996ApJ...470..364E

spaced (every 0.5 day), the integration times varied from 0.8 to 6.4 ks. The two soft (0.1–0.4 and 0.5–0.9 keV) bands, which showed no significant variability during the observations, are apparently dominated by emission from an extended component (e.g., Elvis, Briel, & Henry 1983; Morse et al. 1995). However, the hardest *ROSAT* band (1–2 keV) showed variations significantly in excess of the measured errors.

The *ROSAT* spectra were well fitted by a nonvariable thermal bremsstrahlung ($kT_B = 0.44 \pm 0.05$ keV) component that contributes most of the flux below 1.4 keV and a heavily absorbed ($N_H = 2.3 \times 10^{22}$ cm^{-2}) power law with fixed slope ($\alpha = -0.5$; $S_\nu \propto \nu^\alpha$) and variable normalization ($A = 0.010$–0.024 photons cm^{-2} s^{-1} keV^{-1}) that dominates at medium X-ray energies. However, the proportional counter data have low resolution, and thus a range of other models cannot be ruled out.

The four *ASCA* spectra have higher resolution, allowing more detailed spectral analysis. These data were compatible with a model that includes warm and cold absorbers, thermal bremsstrahlung, a power law, and a 6.4 keV iron line. Again, this is not a unique solution. The iron line shows significant broadening to the redward wing, suggesting a gravitational redshift that would constrain the material to lie very near the black hole (Yaqoob et al. 1995). The 1–2 keV *ASCA* data were used in the light curves along with the *ROSAT* points, with a 10% uncertainty added to account for possible calibration differences. The harder (2–10 keV) *ASCA* data were not used for variability analysis because only four epochs were obtained.

NGC 4151 was continuously observed with the OSSE instrument on *CGRO*. The broadband 50–150 keV count rate showed weak but significant variability. The raw data were calibrated by convolving the detector response function with a model assuming a power law with an exponential cutoff. See Paper III for further details on the X-ray and gamma ray data.

NGC 4151 was near its historical peak brightness during this campaign. The average (absorption-corrected) flux in the 2–10 keV band was 3.6×10^{-10} ergs cm^{-2} s^{-1}. This is bright compared to the compilation of results from *EXOSAT* and *Ginga* reported in Yaqoob et al. (1993), which were in the range $(0.8$–$4) \times 10^{-10}$ ergs cm^{-2} s^{-1}. The mean 1275 Å flux of $\sim 4 \times 10^{-13}$ ergs cm^{-2} s^{-1} Å^{-1} is higher than the range of $(0.4$–$3.6) \times 10^{-13}$ ergs cm^{-2} s^{-1} Å^{-1} seen in 1978–1990 (Edelson, Krolik, & Pike 1990; Palatini & Courvoisier 1994), although the ultraviolet flux was a bit higher during the 1995 March Astro-2 campaign (Kriss et al. 1995).

3. ANALYSIS

3.1. *Variability Amplitudes in Different Wave Bands*

During the period MJD 22.5–32.3, the light curve of NGC 4151 was densely sampled by *IUE*, *ROSAT*, *CGRO*, and ground-based telescopes. The initial analysis of these data involved comparing fractional variability amplitudes during this period as a function of observing frequency. The normalized variability amplitude (NVA, or $F_{\rm var}$) was computed as follows. For each band, the mean ($\langle x \rangle$) and standard deviation ($\sigma_{\rm tot}$) of the flux points and the mean error level ($\sigma_{\rm err}$) were measured. Because the NVA is intended to be free of instrumental effects, it was determined by subtracting in quadrature the measured mean error from the standard deviation and then dividing by the mean flux. That is,

$$F_{\rm var} = \sqrt{\frac{\sigma_{\rm tot}^2 - \sigma_{\rm err}^2}{\langle x \rangle^2}} \,. \quad (1)$$

Note that this is essentially the same procedure used to derive $F_{\rm var}$ in Peterson et al. (1991) and $\sigma_{\rm NVA}$ in Edelson (1992). These quantities are given in Table 2, along with the observing band, number of observations (N), and the difference in days between the first and last observations (ΔT) during this intensive period.

Figure 2 is a plot of NVA as a function of observing wave band. The NVA shows a strong dependence on photon energy, increasing from $F_{\rm var} \approx 1\%$ in the optical to $\sim 4\%$ in the LWP and $\sim 5\%$–9% in the SWP. The variability in the SWP is clearly stronger than at longer wavelengths, but because of the lower variability levels and stronger starlight corrections, it is impossible to say whether the optical and LWP have significantly different "nonstellar NVAs." This strong wavelength dependence has been seen previously in NGC 4151 and other AGN (e.g., Edelson, Krolik & Pike 1990), and is suggestive of the superposition of a nonvariable soft component that dominates in the optical/infrared

TABLE 2

VARIABILITY AMPLITUDE VERSUS BAND

Band	Number of Points	Δt (days)	$\sigma_{\rm tot}$ (%)	$\sigma_{\rm err}$ (%)	$F_{\rm var}$ (%)	$L_{\rm var}$ (10^{40} ergs s^{-1})	$\sigma_{3/4}$ (%)	$\sigma_{1/2}$ (%)
50–150 keV.....	9	8.10	8.9	6.4	6.1	119	...	...
1–2 keV.....	17	9.72	26.5	11.4	23.9	6.7	...	...
0.5–0.9 keV.....	17	9.72	3.5	6.6	...	...	...	...
0.1–0.4 keV.....	17	9.72	3.0	5.0	...	...	...	...
1275 Å	176	9.20	8.6	0.9	8.6	235	8.6	8.6
1330 Å	176	9.20	8.2	1.0	8.2	241	8.1	7.4
1440 Å	176	9.20	6.7	1.5	6.6	179	7.2	6.5
1730 Å	176	9.20	6.1	1.4	6.0	172	5.5	4.1
1820 Å	176	9.20	5.0	1.3	4.8	124	5.1	3.6
1950 Å	176	9.20	4.9	2.0	4.5	106	4.5	3.1
2300 Å	168	9.15	5.3	2.0	4.9	108	3.6	1.9
2688 Å	168	9.15	3.9	1.1	3.7	89	2.7	1.3
4600 Å	17	7.94	1.3	0.9	0.9	23	1.0	0.3
5125 Å	18	9.33	1.1	0.9	0.7	14	0.9	0.2
6200 Å	8	8.91	1.5	0.6	1.4	33	0.6	0.2
6925 Å	8	8.91	1.6	0.7	1.4	36	0.4	0.1

© American Astronomical Society • Provided by the NASA Astrophysics Data System

1996ApJ...470..364E

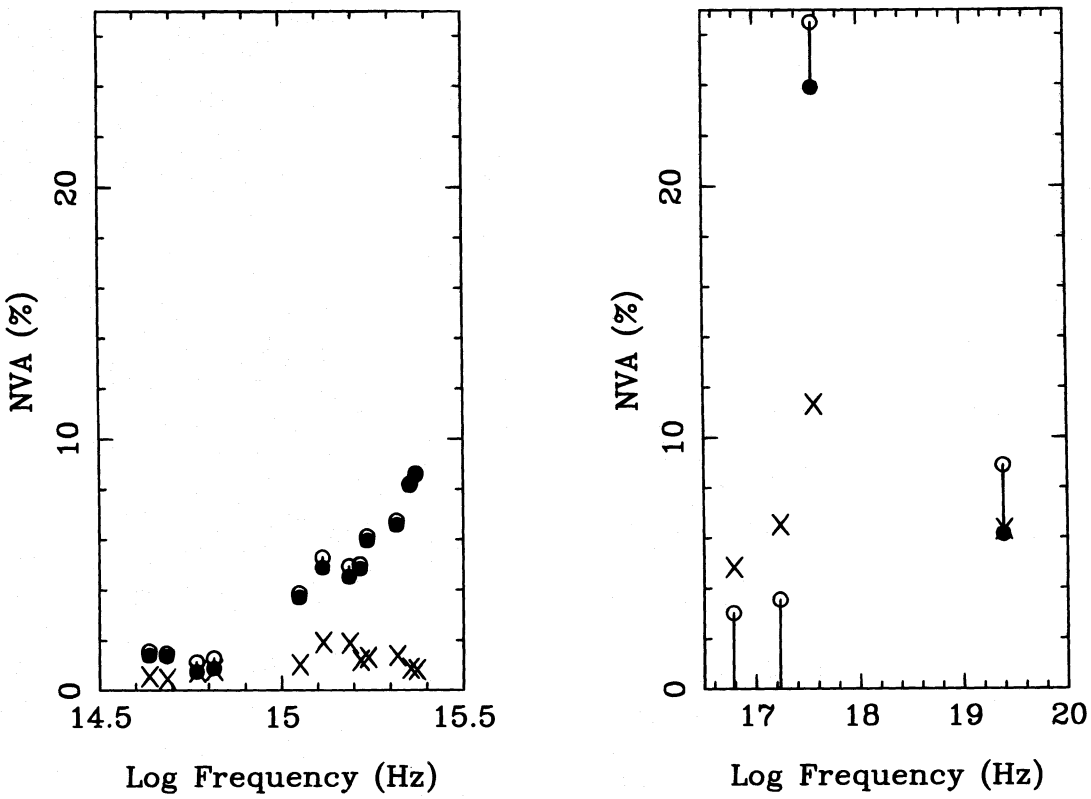

FIG. 2.—Plot of NVA as a function of observing frequency. Note the strong correlation in the optical/ultraviolet band (*left panel*), where the NVA rises from ~1% in the optical to ~9% in the ultraviolet. The open circles refer to the total variability (σ_{tot}), and the filled circles are the NVAs (F_{var}), which represent the variability after correction for instrumental uncertainties (which are denoted by crosses). The strongest NVA is seen in medium-energy (1–2 keV) X-rays (*right panel*), with an NVA of 24%, while there is no significant variability observed in the softer X-ray bands, and weaker variations (NVA = 6%) at 100 keV.

and a variable hard component that dominates in the ultraviolet.

The NVA also shows interesting behavior at high energies. The soft *ROSAT* bands show no evidence for any significant variations, with NVA formally undefined, as the observed variation levels are smaller than the instrumental errors. The medium-energy 1.5 keV X-ray band shows the strongest variability seen in any band, with $F_{var} \approx 24\%$. This large difference is apparently due to the superposition of two components: a soft, extended (and therefore nonvariable) component seen in spectra and *Einstein* high-resolution imager (HRI) images (Elvis et al. 1983), and a harder, strongly variable component. However, this strongly variable component must cut off at some higher energies, because the *CGRO* data show weaker variability, with $F_{var} \approx 6\%$ in the 50–150 keV band.

Unfortunately, there are two important energy ranges in which the variability properties of NGC 4151 during this campaign were not measured: the hard X-ray 2–50 keV gap between *ROSAT* and *CGRO* (the 2–10 keV *ASCA* data cannot be used to measure a meaningful NVA with only four points) and the extreme-ultraviolet 1200 Å (10 eV) to 100 eV gap in the mostly unobservable region between *IUE* and *ROSAT*. The former wave band could contain the bulk of the luminosity of the putative primary emission component, and the latter, the bulk of the disk luminosity. These gaps do limit the power of these data (see § 4), although we note that this campaign has produced the most densely sampled grid in time and energy band obtained of any AGN to date.

Table 2 also gives the monochromatic variable luminosity, defined as $L_{var} = F_{var} \times \nu L_\nu$ (νL_ν is the observed monochromatic luminosity, as defined in § 3.5). This parameter behaves somewhat differently than the NVA. In particular, the medium-energy X-rays, which have the strongest NVA ($F_{var} = 24\%$) actually show the lowest value of L_{var} (6.7×10^{40} ergs s^{-1}). Note, however, that the X-rays appear to be heavily absorbed (~90%–95%; see § 3.5), so the intrinsic value of this quantity is actually much larger.

3.2. *Fluctuation Power Density Spectra*

These are the most densely sampled ultraviolet observations of any AGN obtained to date, allowing examination of the short-timescale variability properties. These data were used to measure the fluctuation power density spectra (PDS) in four ultraviolet bands (1275, 1330, 1820, and 2688 Å), on timescales of ~0.2–5 days. A regular grid of spacing 0.1 day was created, and the value at each point was taken to be the average of the nearest 12 points, weighted as $\exp[(-\Delta T/0.1 \text{ day})^2]$. This resampling, which was necessary to mitigate problems introduced by the periodic ~0.1 day Earth occultation gaps, destroys all information on shorter timescales. However, as seen below, the PDS are dominated by noise on these shorter timescales, so this is not a problem. Only the continuous data were used, and the mean was not subtracted. These resampled data were used to compute the PDS in the four ultraviolet bands, the results of which are shown in Figure 3.

The PDS of AGN show no discrete features that would indicate periodicity. Instead, the fluctuation power is spread

© American Astronomical Society • Provided by the NASA Astrophysics Data System

1996ApJ...470..364E

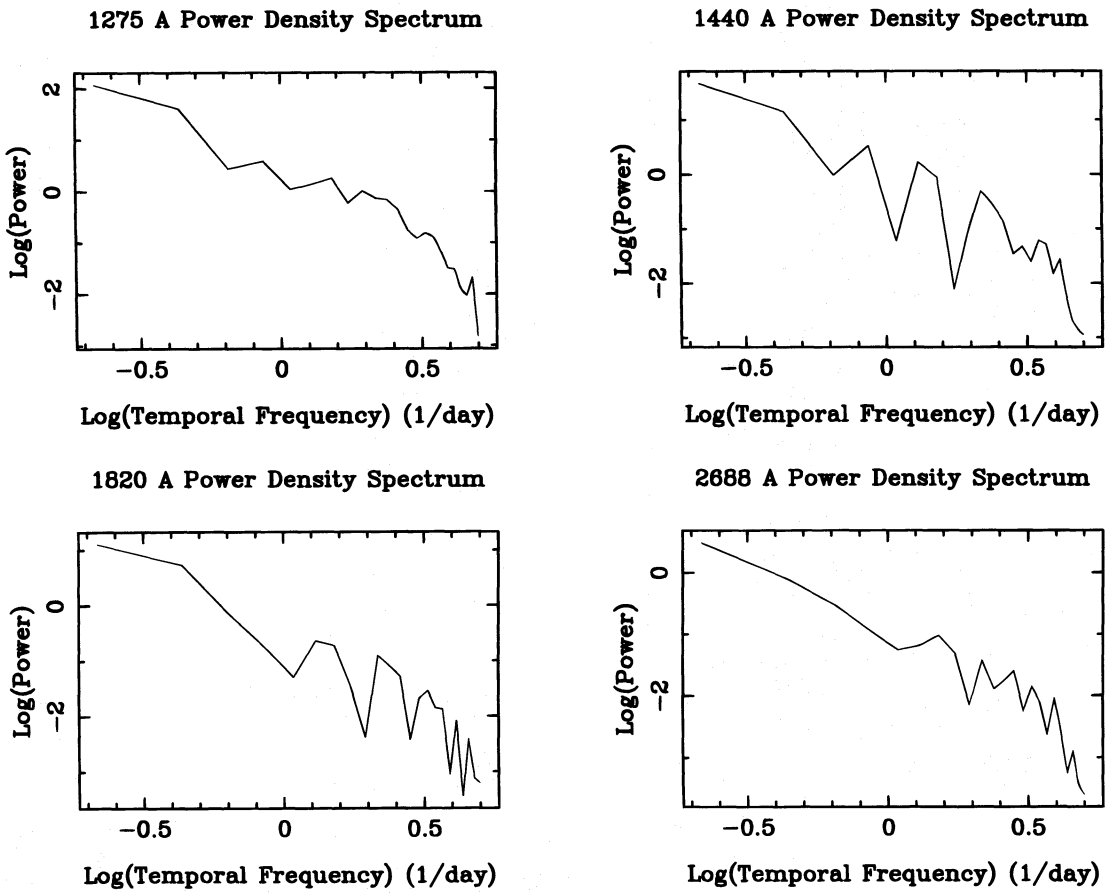

FIG. 3.—PDS of the resampled ultraviolet light curves in four bands. The units of the PDS (*ordinate*) are ergs^2 cm^{-4} Å^{-2}, while the units of the abscissa are days^{-1}. The PDS, which all appear the same to within the errors, show no signs of periodic variability. Instead, they are well fitted by a power law with slope $a \approx -2.5$.

out over a wide range of temporal frequencies. It is common practice to parameterize the PDS of AGN by the function $P(f) \propto f^a$, where $P(f)$ is the PDS at temporal frequency f, and a is the power-law slope. These PDS have $a \approx -2.5$, making them the "reddest" AGN PDS yet measured. In fact, the intrinsic PDS is even redder, as "red-noise leak" makes the observed PD of sources with intrinsic PDS slopes $a < -2$ appear smaller (Papadakis & Lawrence 1995). By comparison, the ultraviolet PDS of NGC 5548 had a slope $a \approx -2$ on timescales of weeks to months (Krolik et al. 1991). This indicates that the variability power is falling off rapidly at short timescales, and the bulk of the variability power is on timescales of days or longer. The X-ray PDS NGC 4151 has $a \approx -2$ timescales of hours to days and $a \approx -1$ on longer timescales (Papadakis & McHardy 1995). The fact that the (rather noisy) X-ray and ultraviolet PDS appear to have different slopes over the same range of timescales may indicate that different processes power the variability at the two wave bands, although systematic differences in the data and reduction techniques for the two data sets make direct comparison difficult.

The four PDS in Figure 3 look similar to within the noise. There do, however, appear to be some qualitative differences in the character of variations in different bands that can be discerned by direct examination of the light curves. In particular, the ultraviolet data give the impression that the most rapid variations occur at the shortest wavelengths, and are somewhat "smeared out" to longer wavelengths. (The ~0.2 day "spikes" in the 2688 Å light curve may be due to instrumental effects.) A similar effect has been seen at longer timescales in *HST* monitoring of NGC 5548 (Korista et al. 1995). Such an effect would not be apparent in the above PDS analysis. However, it is unclear how much of this is intrinsic and how much is due to instrumental differences, since the "variability-to-noise" ratio (that is, $F_{\rm var}/\sigma_{\rm err}$), decreases toward longer wavelengths in the ultraviolet, so that this experiment was less sensitive to rapid variations at longer ultraviolet wavelengths.

3.3. *Zero-Lag Correlation between Wave Bands*

Because there was no measurable interband phase lag (see § 3.4), a slightly different view may be obtained by measuring the zero-lag correlations between variations in different wave bands. To investigate this, fluxes in a number of comparison bands (100 keV, 1.5 keV, 1330 Å, 1820 Å, 2688 Å, and 5125 Å) were correlated with the 1275 Å fluxes. For each of the comparison bands, each flux point was paired with the average of the two 1275 Å flux points measured immediately before and after that point, and 1275 Å uncertainties were taken to be the average of the uncertainties measured for the two data points.

The results are plotted in Figure 4. The number of points (N), linear correlation coefficient (r), Spearman rank correlation coefficient (r_S), t-statistic, and y-intercept are tabulated in Table 3. The 100 keV fluxes ($t \approx 1$) show no correlation with 1275 Å (or with any other band, for that matter). This could suggest that the processes producing the

© American Astronomical Society • Provided by the NASA Astrophysics Data System

1996ApJ...470..364E

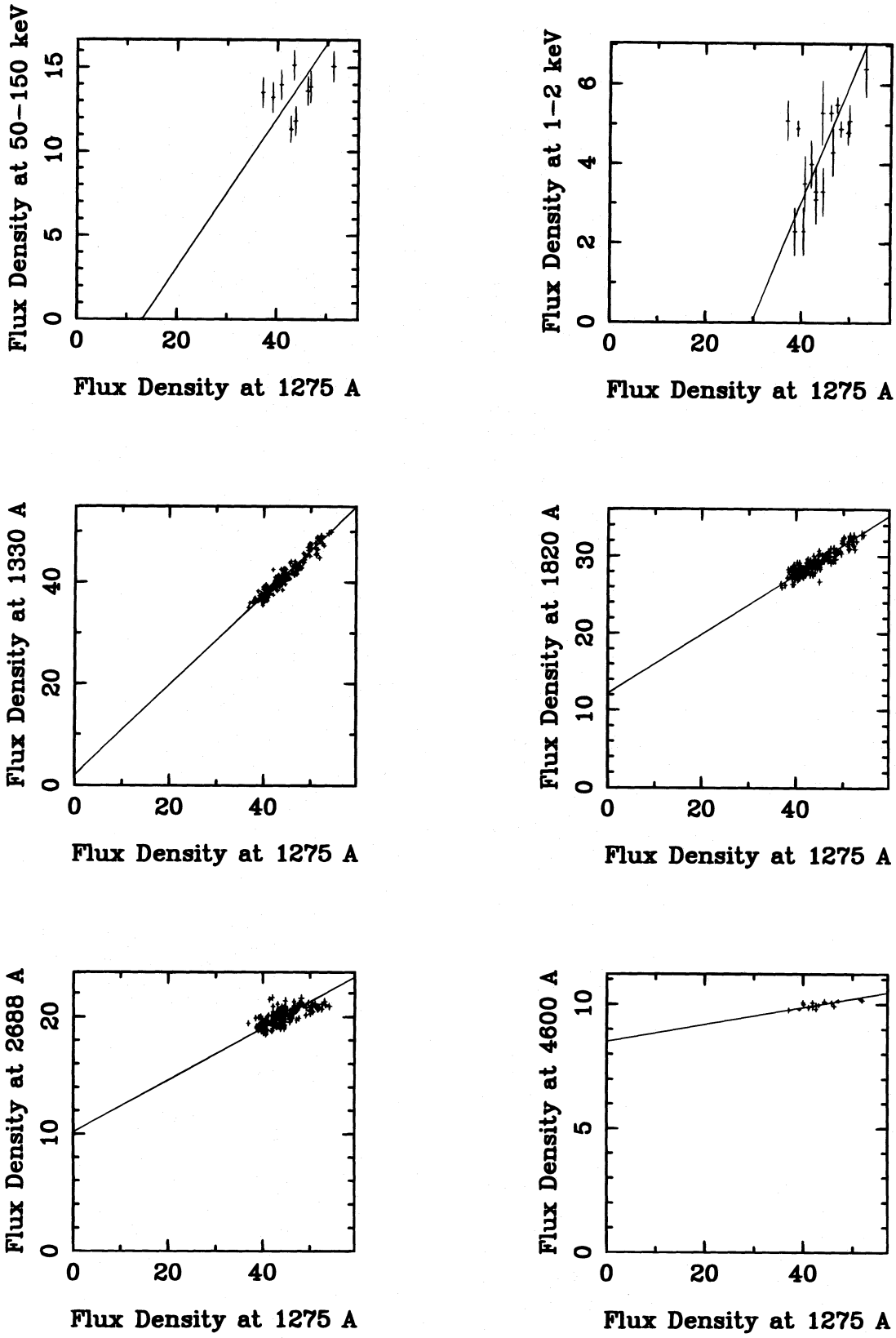

FIG. 4.—Plots of the correlation between continuum fluxes at bands centered on 1275 Å and 100 keV, 1.5 keV, 1330 Å, 1820 Å, 2668 Å, and 5125 Å. The ultraviolet and gamma-ray data are not significantly correlated, but all of the other bands show a significant correlation. The solid lines are unbiased least-squares fits to the data. The regression lines with the long-wavelength ultraviolet have a positive y-intercept, while the ultraviolet–1.5 keV X-ray regression has a positive x-intercept.

© American Astronomical Society • Provided by the NASA Astrophysics Data System

1996ApJ...470..364E

TABLE 3

INTERBAND ZERO-LAG CORRELATION

Band	N	r	r_S	t	y-Intercept
100 keV.....	9	0.33	0.37	1.04	...
1 keV	17	0.60	0.56	2.64	−8.76
1330 Å.....	176	0.96	0.95	38.11	1.93
1820 Å.....	176	0.90	0.86	22.54	12.11
2688 Å.....	168	0.69	0.70	12.47	10.18
5125 Å.....	18	0.65	0.59	2.95	7.21

gamma rays are unrelated to those at work at lower energies, especially given the relatively low NVA of the gamma rays. The data are strongly correlated on these short timescales in all other cases, although the optical and X-ray correlations are a bit marginal, with $t = 2.95$ for 18 points and $t = 2.64$ for 17 points, respectively. Note that Perola et al. (1986) found a similar ultraviolet/X-ray zero-lag correlation in previous data over longer ($\sim$1 yr) timescales, although it was claimed that correlation broke down at the high flux levels seen in this experiment. Following the regression line to zero flux at 1275 Å yields a positive excess at all wave bands except 1.5 keV X-rays. This means that if one models the flux at each wave band as a combination of a nonvariable component and a variable component produced by reprocessing emission from the other wave band, the variable component is always at shorter wavelengths, and the nonvariable component becomes a progressively larger fraction of the total flux as the wavelength increases.

3.4. *Multiwavelength Phase Lags*

The most detailed analysis undertaken with these data was to measure temporal cross-correlation functions between wave bands. If emission in one band is reprocessed to another without feedback, measurement of an interband lag would provide an important confirmation, and indicate which were the primary and secondary bands. This intensive monitoring of NGC 4151 is clearly better suited for this test than any previous campaign. Unfortunately, even in these data, the 1.5 keV X-rays, which show the strongest variations, are clearly undersampled, having been observed at a temporal frequency only one-tenth that in the ultraviolet. The differences between the sampling, variability levels, and signal-to-noise ratios in the different wave bands present problems for measuring the interband lag. Below, a detailed analysis is presented of two independent techniques used to measure the interband correlations and lags: the interpolation and discrete correlation functions.

3.4.1. *The Interpolation Cross-Correlation Method*

Cross-correlation functions were computed using the interpolation cross-correlation function (ICCF) method of Gaskell & Sparke (1986), as subsequently modified by White & Peterson (1994). As described by Gaskell & Peterson (1987), the cross-correlation function was determined by first cross-correlating the real observations from one time series with values interpolated from the second series. The calculation was then performed a second time, using the real values from the second series and interpolated values from the first series. The final cross-correlation function was then taken to be the mean of these two calculated functions. A sampling grid spacing of 0.05 day was used because that is approximately the mean interval between the ultraviolet observations. Because the X-ray and optical continuum light curves are much well sampled than the ultraviolet light curves, the X-ray and optical cross-correlations with the 1275 Å ultraviolet light curve were performed by interpolating only in the ultraviolet light curve. That is, the computed cross-correlation functions are based on the real X-ray and optical points and interpolated (or regularized) ultraviolet points, and no interpolation of the X-ray or optical data was performed.

3.4.2. *The z-Transformed Discrete Correlation Function Method*

The cross-correlation functions for the various continuum bands were similarly calculated by the z-transformed discrete correlation function (ZDCF) method (Alexander 1996), which is related to the discrete correlation function (DCF) of Edelson & Krolik (1988). This method is rather more general than the ICCF, since (*a*) it does not require any assumptions about the continuum behavior between the actual observations and (*b*) it is possible to reject data pairs at zero lag (e.g., two points in different wave bands, measured from one spectrum) and thus avoid false zero-lag correlations that might arise from correlated flux errors. The ZDCF differs in a number of ways from the DCF, a notable feature being that the data are binned by equal population rather than into time bins of equal width $\delta\tau$.

One advantage of this technique is that it allows direct estimation of the uncertainties on the lag without the use of more assumption-dependent Monte Carlo simulations. The maximum likelihood error estimate on the position of the true cross-correlation function peak ($\Delta\tau_{ML}$) is a 68% fiducial confidence interval, meaning that it contains the peaks of 68% of the likelihood-weighted population of all possible cross-correlation functions (Alexander 1996). Phrased more loosely, the confidence interval is where 68% of the cross-correlation functions that are consistent with the ZDCF points are likely to reach their peaks. The accuracy of this error estimate is limited by the assumption that the distributions of the true cross-correlation points around the ZDCF points are independently Gaussian, which is only approximately true, but it does not require any further a priori assumptions about the nature of the variations or transfer function between bands.

3.4.3. *Results*

The various columns in Table 4 give the results obtained by cross-correlating the specified light curve with the 1275 Å light curve. The parameter r_{max} is the maximum value of the cross-correlation function, which occurs at a lag τ_{peak}. Table 4 also gives the centroid of the cross-correlation function, τ_{cent}, which is based on all points with $r \geq 0.5r_{max}$. The computed cross-correlation functions are shown in Figure 5 (ICCF) and Figure 6 (ZDCF).

The measured ranges of $\Delta\tau_{ML}$ of the various bands with 1275 Å (−0.20 to +0.26 day for the 1.5 keV X-rays, −0.14 to +0.01 day for 1820 Å, −0.05, to +0.22 day for 2688 Å, −0.78 to 0.53 day for 5125 Å) are all consistent with zero measurable lag. Thus, we have assigned conservative upper limits on the lags of 1275 Å with 1.5 keV of $\Delta\tau_{ML} \lesssim 0.3$ day, with other ultraviolet bands of $\Delta\tau_{ML} \lesssim 0.15$ day, and with 5125 Å of $\Delta\tau_{ML} \lesssim 1$ day. The physical significance of these limits is discussed in § 4.

3.5. *Broadband Spectral Energy Distributions*

Figure 7 gives a broadband gamma-ray–optical snapshot SED, constructed by combining nearly simultaneous obser-

© American Astronomical Society • Provided by the NASA Astrophysics Data System

1996ApJ...470..364E

TABLE 4

CROSS-CORRELATION RESULTS

Parameter	Method	Soft X-Ray (1–2 keV)	Mid-UV (1820 Å)	Near-UV (2688 Å)	Optical (5125 Å)
r_{max}	ICCF	0.82	0.87	0.70	0.69
	ZDCF	0.71	0.87	0.65	0.57
τ_{peak}(days)	ICCF	−0.25	−0.01	+0.00	−0.05
	ZDCF	+0.07	−0.05	+0.02	−0.05
τ_{cent} (days).....	ICCF	−0.06	−0.04	+0.10	+0.27
	ZDCF	−0.02	−0.08	+0.08	+0.30
$\Delta\tau_{ML}$ (days).....	ZDCF	+0.19, −0.27	+0.06, −0.09	+0.20, −0.07	+0.58, −0.73

vations consisting of the Wise spectrum taken on MJD 25.6, *IUE* spectra LWP 26907 and SWP 49441 taken near MJD 26.0, the *ROSAT* observation centered at MJD 26.0, and *ASCA* observation 1, centered near MJD 26.0. Because of the weak variability and low signal-to-noise ratio in the gamma-ray band, the *CGRO* spectrum was integrated over the entire campaign to produce the high-energy SED. Additional (nonsimultaneous) infrared data from Edelson, Malkan, & Rieke (1987) were used in the spectral fits (§ 4.2) but are not shown in Figure 7. The data plotted are monochromatic luminosities, νL_ν, as a function of frequency, ν.

The quantity νL_ν is given by

$$\nu L_\nu = 4\pi D^2 \nu S_\nu, \quad (2)$$

where S_ν is the flux density and $D = 20$ Mpc is assumed to be the distance to NGC 4151 (Tully 1988).

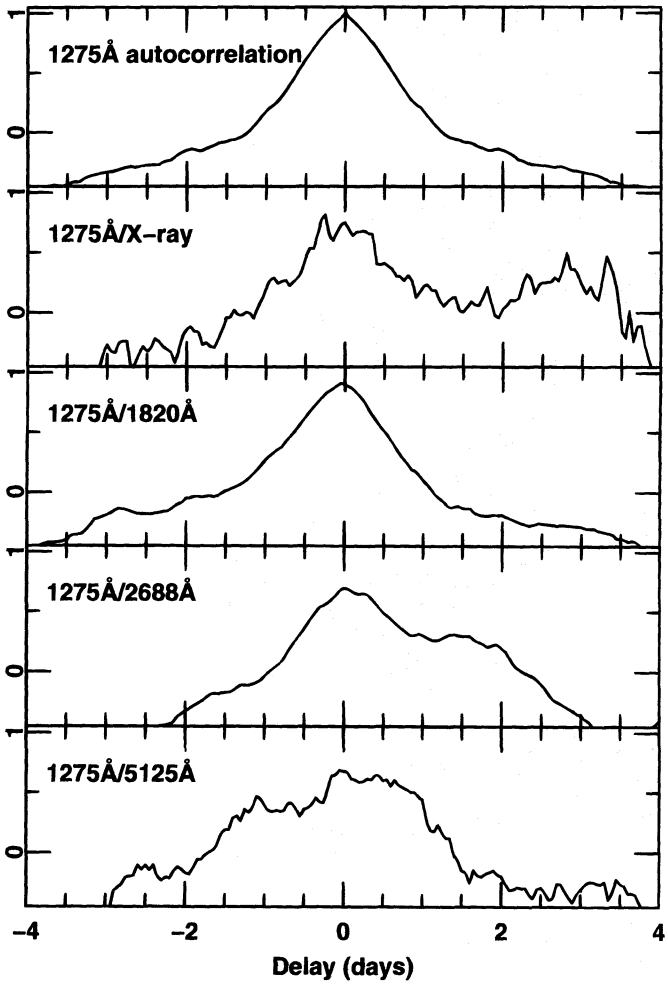

FIG. 5.—Interpolated cross-correlation functions between 1275 and 1275 Å (*top panel*; autocorrelation), 1.5 keV (*second panel*), 1820 Å (*third panel*), 2688 Å (*fourth panel*), and 5125 Å (*bottom panel*). In all cases the peaks are consistent with zero lag.

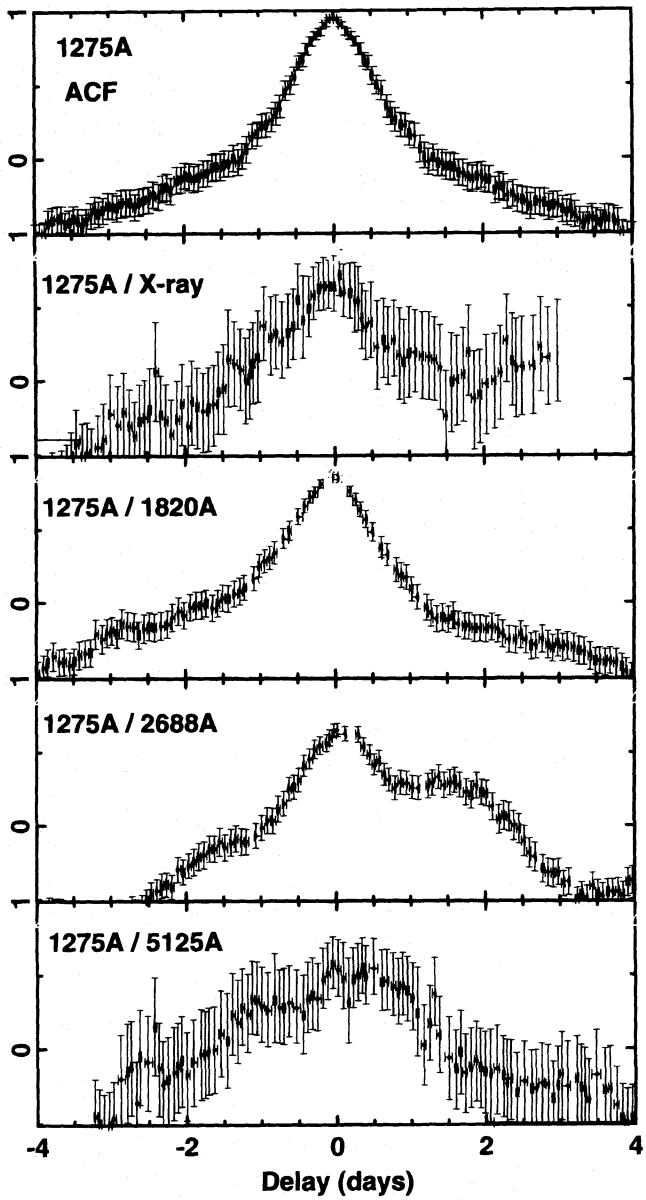

FIG. 6.—Discrete cross-correlation functions between 1275 and 1275 Å (*top panel*; autocorrelation), 1.5 keV (*second panel*), 1820 Å (*third panel*), 2688 Å (*fourth panel*), and 5125 Å (*bottom panel*). In all cases the peaks are consistent with zero lag.

© American Astronomical Society • Provided by the NASA Astrophysics Data System

1996ApJ...470..364E

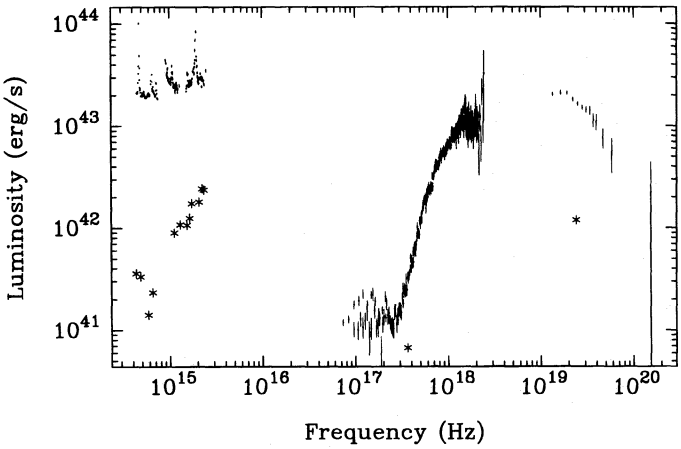

FIG. 7.—Spectral energy distribution of NGC 4151. Plotted quantities are monochromatic luminosity ($4\pi D^2 \nu S_\nu$) as a function of frequency. Optical, ultraviolet, X-ray, and gamma-ray data are taken from observations made near MJD 26. The asterisks show the rms variability in the observing bands listed in Table 2, in terms of monochromatic luminosity.

The SED of any Seyfert 1 galaxy is of course a combination of a number of components, and in particular we note that starlight from the underlying Sab galaxy of NGC 4151 contributes a significant amount of the optical/infrared flux. Peterson et al. (1995) estimated that the underlying galaxy produced a flux of 19 mJy at 5125 Å in the 10″ × 15″ Wise aperture, in good agreement with the independent result reached in Paper II of this series. This corresponds to approximately 25% of the 5125 Å flux at the light levels seen in this campaign, so the 5125 Å NVA of the nuclear component (excluding starlight) is approximately 1.33 times the observed value quoted in Table 2. For a normal Sab galaxy, approximately 42% of the light at 6925 Å, 31% of the light at 6200 Å, 21% of the light at 4600 Å, and 4% of the light at 2688 Å would be due to starlight.

Finally, we note one other important feature in the SED: The soft X-rays show significant absorption due to line-of-sight gas intrinsic to NGC 4151 (evident below 4 keV) and in our own Galaxy (evident below 0.3 keV). Spectral fits indicate that approximately 90%–95% of the 1–2 keV luminosity appears to have been absorbed by gas along the line of sight (see Paper III for details), although this result is model dependent. This would imply that the intrinsic 1–2 keV luminosity is 10–20 times that observed. Possible sources of the intrinsic absorption include partial covering by cold gas (e.g., Holt et al. 1980; Yaqoob, Warwick, & Pounds 1989; Yaqoob et al. 1993) or absorption in a warm, ionized medium (Weaver et al. 1994a; 1994b; Warwick, Done, & Smith 1996). Similar behavior has been seen in the SED of NGC 3783 obtained during the "World Astronomy Day" campaign (Alloin et al. 1995). A smaller fraction (~35%) of the 2–10 keV flux is apparently absorbed, but unfortunately the data are inadequate to characterize the variability in this band.

3.6. *Summary of Observations*

NGC 4151 was monitored intensively with *IUE*, *ROSAT*, *ASCA*, *CGRO*, and ground-based optical telescopes for ~10 days in 1993 December. These observations provided the most intensively sampled multiwavelength light curve of an AGN to date. The major new observational results are as follows:

1. NGC 4151 showed strong variability from the optical through gamma-ray bands during this period. The optical/ultraviolet/X-ray light curves are similar but not identical, with no detectable lags between variations in the different bands. The upper limits on the lags are, between 1275 Å and 1.5 keV, $\lesssim$0.3 day; between 1275 and 5125 Å, $\lesssim$1 day; and between 1275 Å and the other ultraviolet bands, $\lesssim$0.15 day. The 100 keV variations are not clearly related to those in any other band.

2. The strongest variability was seen in the medium-energy X-rays, with the 1–2 keV band showing an NVA of 24%. The variations were systematically weaker at lower energies, with NVAs of 9%, 5%,4%, and 0.5% at 1275, 1820, 2688, and 5125 Å, respectively. However, the 100 keV light curve showed an NVA of only 6%, and the soft (<1 keV) X-rays showed no detectable variability. The observed luminosity (as opposed to fractional) variability was seen to be lowest in the 1.5 keV band, apparently due to strong X-ray absorption along the line of sight.

3. The PDS of all four ultraviolet bands are similar, showing no evidence for periodicity, but instead being well modeled as a power law with $P(f) \propto f^{-2.5}$. The intrinsic slope is even steeper, making the short-timescale ultraviolet PDS of NGC 4151 the reddest AGN PDS observed to date.

4. The broadband SED shows a strong deficit in the soft/mid–X-ray, which is well fitted as a factor of ~15 absorption by gas on the line of sight.

Finally, the character of the multiwavelength variability in the Seyfert 1 NGC 4151 appears to differ markedly from the only other AGN monitored with similar intensity. The BL Lac object PKS 2155−304 was observed continually for ~3 days at ultraviolet (Urry et al. 1993), X-ray (Brinkmann et al. 1994), and optical (Courvoisier et al. 1995) wave bands. Multiwavelength analysis by Edelson et al. (1995) found that the X-ray, ultraviolet, and optical variations were almost identical in amplitude and shape, but that the X-ray variations led those in the ultraviolet and optical by ~2–3 hr. For these observations of NGC 4151, and other Seyfert 1s observed over longer timescales (e.g., Clavel et al. 1991), the light curves do show significant differences between wave bands, with NVA a strong function of energy, but no lag has been measured between variations at different bands. This is an observed (and therefore model-independent) example of an intrinsic difference between Seyfert 1s and BL Lac objects.

4. DISCUSSION

These results have important implications for models that attempt to explain the ultraviolet emission from AGN. There are currently two broad classes of such models. The first hypothesizes that the bulk of the ultraviolet luminosity is produced internally by viscosity in the inner regions of an accretion disk surrounding a central black hole, and the second that the observed ultraviolet emission is produced in gas illuminated and heated by the source that we observe at high energies. Of course, the true picture could be a combination of these processes, a hybrid in which both intrinsic emission from an accretion disk and reprocessing of X-ray emission are important (and, indeed, may feed back upon each other), or, conversely, it may be that neither of these models is relevant.

© American Astronomical Society • Provided by the NASA Astrophysics Data System

1996ApJ...470..364E

4.1. *Mass and Size Scales*

Although the specific processes responsible for AGN emission have not been clearly identified, there is broad support for the general model of a black hole and accretion disk (see § 1). In this model, the emission from normal (nonblazar, radio-quiet) Seyfert 1s like NGC 4151 is relatively isotropic, not significantly Doppler-boosted or beamed toward Earth. In this case, it is possible to use variability to place relatively model-independent limits on the central black hole mass (and therefore the size scale).

The most general is the Eddington limit, which requires only that the source be stable, gravitationally bound, and possess a high degree of spherical symmetry. The minimum central mass given by this limit is

$$M_{\rm E} = \frac{L_{\rm E}\sigma_e}{4\pi G c m_p}, \tag{3}$$

where $L_{\rm E}$ and $M_{\rm E}$ are the Eddington luminosity and mass, σ_e is the Thomson cross section, and m_p is the proton mass. Since the integrated luminosity of NGC 4151 is $\sim 4 \times 10^{43}$ ergs s^{-1}, the Eddington mass is $M_{\rm E} \approx 3 \times 10^5\ M_\odot$.

For a source surrounding a black hole of mass $M_{\rm BH}$, and Schwarzschild radius $R_{\rm S}$, the minimum variability timescale ($t_{\rm min}$) can be estimated from the size ($r_{\rm min}$) of the smallest stable orbit, which is

$$r_{\rm min} \approx c t_{\rm min} \approx 3R_{\rm S} \approx 6GM_{\rm BH}/c^2 \tag{4}$$

for a Schwarzschild black hole. For $M_{\rm BH} \gtrsim M_{\rm E} \approx 3 \times 10^5\ M_\odot$, this implies $r_{\rm min} \gtrsim 3 \times 10^{11}$ cm or $t_{\rm min} \gtrsim 10$ s, which is not a significant constraint on data which were sampled every hour.

A larger but more model-dependent constraint assumes Keplerian orbits and uses the correlation between the widths of emission lines and the distances estimated from their lags to estimate the central mass. In the form in which this estimate is generally presented, the inferred mass is the true mass if the clouds travel on circular orbits. If the clouds are gravitationally bound, but nongravitational forces (e.g., radiation pressure or hydrodynamics) affect cloud motions, the real mass is greater than this estimate; if the motions are unbound, the real mass is smaller than this estimate. Clavel et al. (1987, 1990) used this method to derive a central mass of $M \approx 4 \times 10^7\ M_\odot$ for NGC 4151. This corresponds to a smallest stable orbit of $r_{\rm min} \approx 4 \times 10^{13}$ cm ≈ 20 lt-minutes. Again, this relatively weak constraint is not significant for these data.

4.2. *Thermal Accretion Disk Models*

If the ultraviolet/optical continuum is optically thick thermal emission, the variability amplitudes can be used to constrain the temperature distribution. The simplest nontrivial general case is a flat, azimuthally symmetric disk with a local blackbody temperature that drops with radius as some power law: $T(r) = T_0(r/r_0)^{-\alpha}$. When $\alpha = \frac{3}{4}$, this is a fair approximation of a standard accretion disk, except at the smallest radii. By contrast, in a disk that radiates predominantly by reprocessed energy (see § 4.3), α can be smaller, depending on the geometry of both the disk and the source of the primary radiation. If the local emission is described by a blackbody, the contribution of an annulus to the total disk flux density at a given frequency ν is

$$S_\nu \propto \int_{x_1}^{x_2} \frac{x^{2/\alpha - 1}}{e^{-x} - 1}\, dx, \tag{5}$$

where $x = h\nu/kT(r)$, and the starting and ending points of the integral are defined by the temperatures at the inner and outer radii of the ring. The increasing amplitude of variations with observing frequency is then naturally attributed to changing emission from the hotter regions (that is, the inner disk radii).

There is a test of the simplest case that produces simultaneous multiwavelength variations, in which the emission from the outer disk ($x > x_2$) is constant, and all of the variability is produced by a complete, simultaneous modulation of the emission from the inner disk ($0 < x < x_2$). The only free parameter is the radius that separates the variable and constant parts of the disk, and this can be determined from the NVA at a single wavelength. For example, using the 1275 Å variability amplitude of 8.6% gives $x_2 = 0.50$ for $\alpha = \frac{3}{4}$ or $x_2 = 1.38$ for $\alpha = \frac{1}{2}$. This corresponds to a boundary at the disk rdius, where the temperature is 215,000 or 78,000 K, respectively. The last two columns of Table 2 show how the percentage flux would increase if all of the emission inside this radius (the putative variable component) doubled, including the effects of starlight. There is good agreement between the simple thermal model and the observed wavelength dependence of the variability amplitude for the standard accretion disk case, $\alpha = \frac{3}{4}$. This is not a strong function of how the inner boundary is chosen; for the $\alpha = \frac{1}{2}$ case, truncating the integration to between $x_1 = 0.7$ and $x_2 = 1.38$ changes the result by only 20%.

The success of this simple exercise motivated the fitting of the ultraviolet/optical SED with a standard model of a geometrically thin, optically thick accretion disk (e.g., following the formalism of Sun & Malkan 1989). Aside from the starlight, no additional long-wavelength component was included in the models, so no attempt was made to fit fluxes longward of 2 μm. If the disk is assumed to be viewed face-on, and the black hole is spinning rapidly (Kerr metric), the best-fit model parameters are $M_{\rm BH} = 1 \times 10^8\ M_\odot$ and $\dot{M} = 0.01\ M_\odot\ {\rm yr}^{-1}$. If, on the other hand, the black hole is assumed stationary (Schwarzschild metric), the best-fit parameters are $M_{\rm BH} = 4 \times 10^7\ M_\odot$ and $\dot{M} = 0.025\ M_\odot\ {\rm yr}^{-1}$. In either case, the accretion rate corresponds to 0.6% of the Eddington rate. The black hole mass inferred from the Schwarzschild fit agrees with the Keplerian vaue obtained by Clavel et al. (1987, 1990). These fits give higher weight to the higher signal-to-noise optical continuum than to the ultraviolet continuum where the disk light dominates, which in turn requires a hotter disk and consequently a lower black hole mass [(1–2) $\times 10^7\ M_\odot$]. All the disk fits would give significantly larger black hole masses if the disk had a nonzero inclination.

Integrating the multi–wave-band disk emission out to a boundary radius of $R \approx 2 \times 10^{14}$ cm ≈ 0.07 lt-day shows that approximately 30%, 20%, and 5% of the total disk flux at 1275, 2688, and 5125 Å, respectively, is produced in the inner disk. (These numbers refer to the Kerr model, but are not very model dependent; Malkan 1991.) After correcting for the effects of Galactic starlight in the $\sim 10''$ aperture, the 5125 Å emission from the inner disk falls to $\sim 4\%$. For $M_{\rm BH} \approx (0.4\text{–}1) \times 10^8\ M_\odot$, this radius corresponds to

© American Astronomical Society • Provided by the NASA Astrophysics Data System

1996ApJ...470..364E

$R \approx 6$–$15\ R_S$. These tractions are approximately the same as the largest peak-to-peak variations observed in these bands during the intensive 10 day multi–wave-band monitoring campaign. Thus, one consistent explanation for the decline in variability with increasing wavelength is that the variations occur entirely inside the inner disk. At a distance ≈ 0.07 lt-day from a $4 \times 10^7\ M_\odot$ black hole, the orbital timescale is ~ 1 day, whereas the dominant fluctuations clearly occur on longer timescales (i.e., the 1275 Å peak-to-peak variation was only 42% over the entire 10 day intensive campaign). Thus, they could be associated with either orbital mechanics or thermal fluctuations in the inner disk. It must also be noted that this simple disk model does not produce any X-ray emission, although this is also likely to originate within the inner regions.

4.3. *Reprocessing Models*

These data also can be used to constrain models in which the ultraviolet radiation is produced in gas that is heated by the same X-ray continuum that we observe directly at higher energies. In this model, time variations in the ultraviolet and high-energy fluxes should be closely coupled: the ultraviolet becomes stronger shortly after the high-energy flux rises, and the high-energy flux may itself respond to changes in the ultraviolet flux if the ultraviolet photons provide seeds for Compton upscattering into the higher energy band. The delays in both cases are essentially due to the light-travel time between the two source regions. Consequently, the (reprocessed) ultraviolet emission should vary simultaneously with the (primary) X-rays on timescales longer than the round-trip light-travel time between the emitting regions (e.g., Clavel et al. 1992). The strong correlation between the ultraviolet and X-ray variations therefore supports the reprocessing hypothesis. The lack of any lag within the ultraviolet could be explained in two ways: either the subregions responsible for variations in different wavelengths are likewise very close to each other, or, as with the accretion disk model, only the hottest part of the region is varying. In the context of this model, the lack of any detectable lag implies that the X-ray–and ultraviolet-emitting regions are separated by $\lesssim 0.15$ lt-day ($\frac{1}{2} \times 0.3$ lt-day, because the light must travel in both directions), so the bulk of the reprocessing must occur in the central regions. Perola & Piro (1994) applied a more detailed reprocessing model to earlier X-ray/ultraviolet observations and predicted that high time resolution monitoring would measure lags of order 0.03–0.1 day (rather close to, but still formally consistent with, the measured limits of $\lesssim 0.15$–0.3 day).

The reprocessing model is supported by the broad profile of the iron Kα line, which suggests relativistic effects associated with an origin very close to a central black hole (Yaqoob et al. 1995). However, the *ASCA* observations (and previous medium-energy X-ray observations) found no evidence for any significant "hard tail" in the X-ray spectrum (Paper III; Maisack & Yaqoob 1991). While the presence of the iron line implies reprocessing by some material, the lack of a "reflection hump" suggests that the material is not optically thick to Compton scattering, as would be expected in the putative reprocessing disk.

An associated problem is the overall energy budget. The total X-ray/gamma-ray flux must be adequate to produce the observed ultraviolet/optical/infrared flux, and the variable high-energy flux must also equal or exceed that at lower energies. The observed, integrated 0.1–1 μm flux is $\sim 11 \times 10^{-10}$ ergs cm^{-2} s^{-1}. Because strong Lyα and C IV emission indicates that the ultraviolet bump extends to wavelengths substantially shorter than 1000 Å, the intrinsic, integrated flux is probably larger by a factor of ~ 3, corresponding to a total ultraviolet/optical/infrared flux of order 30×10^{-10} ergs cm^{-2} s^{-1}. The observed, integrated 1–2 and 2–10 keV fluxes are $\sim 0.05 \times 10^{-10}$ and $\sim 2.4 \times 10^{-10}$ ergs cm^{-2} s^{-1}, respectively. After correction for line-of-sight absorption (which is particularly important at 1–2 keV), the intrinsic, integrated fluxes rise to $\sim 0.9 \times 10^{-10}$ and $\sim 3.6 \times 10^{-10}$ ergs cm^{-2} s^{-1}, for a total of $\sim 4.5 \times 10^{-10}$ ergs cm^{-2} s^{-1}. This is not adequate to power the lower energies, but inclusion of the *CGRO* data and interpolating between *ASCA* and *CGRO* yields a (rather uncertain) integrated 1–200 keV flux of order (15–20) $\times 10^{-10}$ ergs cm^{-2} s^{-1}. This would be of the order of the amount necessary to power the lower energies. However, the fact that the gamma-ray variations differ from those in all other wave bands suggests that the bulk of the 10–200 keV emission (which dominates the X-ray/gamma-ray flux) arises in a component that does not fully participate in the reprocessing. In this case, the X-ray/gamma-ray luminosity would still be a factor of order 3 too small, so at most $\sim \frac{1}{3}$ of the observed infrared/optical/ultraviolet flux could be due to reprocessing. However, this cannot be independently verified because the *ASCA* sampling above 2 keV is inadequate to characterize the variability, and indeed the entire 10–50 keV spectrum is interpolated, not observed.

Although the absolute X-ray luminosity changes are observed to be small compared to those in the ultraviolet/optical, spectral fits indicate that the X-rays are highly (a factor of ~ 15–20) absorbed, and the intrinsic, absorption-corrected variations have more than enough power to drive the ultraviolet/optical variations. However, the NVA, which measures the fractional (as opposed to absolute) variations, is 24% in the X-rays, while it is only 9%, 5%, 4%, and 1% at 1275, 1820, 2688, and 5125 Å, respectively. This indicates that at most 35%, 20%, 15%, and 4% of the emission at 1275, 1820, 2688, and 5125 Å could be due to reprocessing, with the rest coming from a component with different (slower) variability. As with the previous analysis, this would indicate that at most $\sim \frac{1}{3}$ of the ultraviolet/optical/infrared can be reprocessed emission from higher energies.

4.4. *Summary*

This campaign, the most intensive sampling of any AGN made to date, has yielded important constraints on the physical conditions and processes producing the emission from NGC 4151.

1. NGC 4151 showed significant variability over timescales of days, so the emitting region must be smaller than of order a few light-days across, assuming the emission is not beamed. The limits on the interband lags indicate that, if there is reprocessing of flux between bands, none of the emission regions could be larger than ~ 0.15 lt-day. The lower limit to the central black hole mass derived from the Eddington limit is small ($M_{\rm BH} \gtrsim 3 \times 10^5\ M_\odot$), corresponding to a minimum variability time of only 10 s, which is not a significant constraint.

2. Accretion disk fits to the SED yield a central black hole with a mass of $(0.4$–$1) \times 10^8\ M_\odot$, accreting well below the Eddington limit. The fact that the low NVAs decrease from medium-energy X-ray to ultraviolet to optical wave

© American Astronomical Society • Provided by the NASA Astrophysics Data System

1996ApJ...470..364E

bands is consistent with the accretion disk model if the bulk of the variable ultraviolet/optical emission originates in a region ~ 0.07 lt-day ($\sim 10R_S$) from the center. This model gives no immediate explanation of the link between ultraviolet and X-ray variations.

3. The reprocessing model predicts a strong correlation between ultraviolet and X-ray variability, which is observed. Because the NVAs become systematically smaller at longer wavelengths, and because the absorption-corrected X-ray/gamma ray luminosity is only much smaller than in the ultraviolet/optical/infrared, at most $\sim \frac{1}{3}$ of the lower energy emission could be produced by reprocessing.

This suggests that perhaps the ultraviolet arises in a disk powered partially by illumination by an X-ray source and partially by internal viscosity and accretion. Determining the exact mix of these emission components will require probing the ultraviolet/X-ray bands at the shortest accessible timescales. It is of particular importance to extend the coverage to the gap at X-ray energies harder than 2 keV. This is the goal of the just completed coordinated *X-Ray Timing Explorer* (*XTE*)/*IUE*/ground-based observations of NGC 7469, scheduled for the middle of 1996, and it is hoped that they will shed further light on this important question.

The work of B. M. P. was supported by NASA grants NAGW-3315 and NAG 5-2477. The work of D. M. C. and the *IUE* data reduction were supported by NASA ADP grant S-30917-F. The work of A. V. F. and L. C. H. was supported by NSF grant AST 89-57063. This research has also been supported in part by NASA grants NAG 5-2439, NAG 5-1813, and NAGW-3129.

REFERENCES

Alexander, T. 1996, preprint
Alloin, D., et al. 1995, A&A, 293, 293
Ayres, T. 1993, PASP, 105, 538
Barvainis, R. 1987, ApJ, 350, 537
Brinkmann, W., et al. 1994, A&A, 288, 433
Clavel, J., et al. 1987, ApJ, 321, 251
Clavel, J., et al. 1990, MNRAS, 246, 668
Clavel, J., et al. 1991, ApJ, 366, 64
Clavel, J., et al. 1992, ApJ, 393, 113
Collin-Souffrin, S. 1991, A&A, 249, 344
Courvoisier, T., et al. 1995, ApJ, 438, 108
Crenshaw, D. M., et al. 1996, ApJ, 470, 322 (Paper I)
Edelson, R. A. 1992, ApJ, 401, 516
Edelson, R. A., & Krolik, J. H. 1988, ApJ, 333, 646
Edelson, R., et al. 1995, ApJ, 438, 120
Edelson, R. A., Krolik, J. H., & Pike, G. F. 1990, ApJ, 359, 86
Edelson, R. A., Malkan, M., & Rieke, G. 1987, ApJ, 321, 233
Elvis, M., Briel, V., & Henry, J. P. 1983, ApJ, 268, 105
Gaskell, C. M., & Peterson, B. M. 1987, ApJS, 65, 16
Gaskell, C. M., & Sparke, L. S. 1986, ApJ, 305, 175
George, I. M., & Fabian, A. C. 1991, MNRAS, 249, 352
Guilbert, P. W., & Rees, M. J. 1988, MNRAS, 233, 475
Haardt, F., & Maraschi, L. 1993, ApJ, 413, 507
Haardt, F., Maraschi, L., & Ghisellini, G. 1994, ApJ, 432, L95
Holt, S. S., Mushotzky, R. F., Becker, R. H., Boldt, E. A., Serlemitsos, P. J., Szymkowiak, A. E., & White, N. E. 1980, ApJ, 241, L13
Kaspi, S., et al. 1996, ApJ, 470, 336
Korista, K. T., et al. 1995, ApJS, 97, 285
Kriss, G. A., Davidsen, A. F., Zheng, W., Kruk, J. W., & Espey, B. R. 1995, ApJ, 454, L7
Krolik, J. H., Horne, K., Kallman, T. R., Malkan, M. A., Edelson, R. A., & Kriss, G. A. 1991, ApJ, 371, 541
Lightman, A. P., & White, T. R. 1988, ApJ, 335, 57
Maisack, M., & Yaqoob, T. 1991, A&A, 249, 25
Malkan, M. A. 1983, ApJ, 268, 582
Malkan, M. A. 1991, in Structure and Emission Properties of Accretion Disks, ed. C. Bertout, S. Collin-Souffrin, J.-P. Lasota, & J. Tran Thanh Van (Gif-sur-Yvette: Editions Frontières), 165
Malkan, M. A., & Sargent, W. L. W. 1982, ApJ, 254, 22
Matt, G., Fabian, A. C., & Ross, R. R. 1993, MNRAS, 262, 179
Molendi, S., Maraschi, L., & Stella, L. 1992, MNRAS, 255, 27
Morse, J. A., Wilson, A. S., Elvis, M., & Weaver, K. A. 1995, ApJ, 439, 121
Nandra, K., Pounds, K. A., Stewart, G. C., George, I. M., Hayashida, K., Makino, F., & Ohasi, T. 1991, MNRAS, 248, 760
Palatini, S., & Courvoisier, T. J.-L. 1994, A&A, 291, 74
Papadakis, I. E., & Lawrence, A. 1995, MNRAS, 272, 161
Papadakis, I. E., & McHardy, I. M. 1995, MNRAS, 273, 923
Penton, S., et al. 1996, in preparation
Perola, G., & Piro, L. 1994, A&A, 281, 7
Perola, G., et al. 1986, ApJ, 306, 508
Peterson, B. M., et al. 1995, PASP, 107, 579
Peterson, B. M., et al. 1991, ApJ, 368, 119
Rees, M. J. 1984, ARA&A, 22, 471
Rokaki, E., Collin-Souffrin, S., & Magnan, C. 1993, A&A, 272, 8
Rokaki, E., & Magnan, C. 1992, A&A, 261, 41
Sanders, D. B., Phinney, E. S., Neugebauer, G., Soifer, B. T., & Matthews, K. 1989, ApJ, 347, 29
Shields, G. 1978, Nature, 272, 706
Sun, W.-H., & Malkan, M. A. 1989, ApJ, 346, 68
Tully, R. B. 1988, Nearby Galaxies Catalogue (Cambridge: Cambridge Univ. Press)
Ulrich, M.-H., Boksenberg, A., Bromage, G. E., Clavel, J., Elvius, A., Penston, M. V., Perola, G. C., & Snijders, M. A. J. 1991, ApJ, 382, 483
Urry, C. M., et al. 1993, ApJ, 411, 614
Warwick, R. S., Done, C., & Smith, D. A. 1995, MNRAS, 275, 1003
Warwick, R. S., et al. 1996, ApJ, 470, 349 (Paper III)
Weaver, K. A., et al. 1994a, ApJ, 423, 621
Weaver, K. A., Yaqoob, T., Holt, S. S., Mushotzky, R. F., Matsuoka, M., & Yamauchi, M. 1994b, ApJ, 436, L27
White, R. J., & Peterson, B. M. 1994, PASP, 106, 879
Yaqoob, T., et al. 1993, MNRAS, 262, 435
Yaqoob, T., Edelson, R. A., Weaver, K. A., Warwick, R. S., Mushotzky, R. F., Serlemitsos, P. J., & Holt, S. S. 1995, ApJ, 453, L81
Yaqoob, T., Warwick, R. S., & Pounds, K. 1989, MNRAS, 236, 153
Zdziarski, A., Ghisellini, G., George, I. M., Svensson, R., Fabian, A. C., & Done, C. 1990, ApJ, 363, L1

© American Astronomical Society • Provided by the NASA Astrophysics Data System